FDR4LDYN
Fundamental Data Record for Land Dynamic
ESA RFP/3-18440/24/I-DT-I

Algorithm Theoretical Basis Document (ATBD)
DT2-1

Revision History

Revision	**Date**	**Author(s)**	**Description**
0.1	20 June 2025	TU Wien	Preliminary version

How to cite this document

ESA, *Algorithm Theoretical Basis Document (ATBD) ERS ESCAT Fundamental Data Record for Land Dynamics v1.0 12.5 km sampling*, v0.1, 2025

Table of Contents

1 Executive summary

The Algorithm Theoretical Basis Document (ATBD) provides a comprehensive description of the retrieval methods and processing chain used to generate the FDR4LDYN data products. These products are derived from C-band backscatter observations collected by the scatterometers (ESCAT) on board the European Remote Sensing satellites ERS-1 and ERS-2. The core variables provided are normalized backscatter, slope, and curvature, complemented by ancillary parameters such as yearly azimuthal correction terms and uncertainty estimates. Multiple variants of the slope and curvature time series are included in the FDR4LDYN data products to address different application requirements. The data record is designed to ensure optimal interoperability with the corresponding current Metop ASCAT and future Metop-SG SCA backscatter observables, supporting the creation of a consistent long-term record of land surface backscatter. The FDR4LDYN products enable the monitoring of land surface dynamics and support diverse scientific and operational applications in domains such as soil moisture estimation, vegetation dynamics, flood monitoring, cryospheric research, and climate studies.

2 Introduction

2.1 Purpose of the document

The Algorithm Theoretical Basis Document (ATBD) is intended to provide a detailed description of the scientific background and theoretical justification behind the algorithm utilized for the FDR4LDYN data products based on C-band backscatter observations collected by the scatterometers (ESCAT) onboard the European Remote Sensing satellites ERS-1 and ERS-2.

2.2 Targeted audience

This document mainly targets:

1. Remote sensing experts interested in the retrieval and error characterization of satellite backscatter observable data sets.
2. Users of backscatter, slope, and curvature data sets who want to obtain a more in-depth understanding of the algorithm and sources of error.

3 ESCAT on-board ERS-1 and ERS-2

3.1 ERS missions

The first European Remote Sensing satellite, ERS-1, was launched by ESA on 17 July 1991 from Kourou, French Guiana [1]. As a major precursor to Europe's current Earth observation missions, ERS-1 built upon development efforts and feasibility studies initiated in the early 1970s [2]. ERS-1 carried a suite of instruments designed for comprehensive environmental monitoring of land, water, ice, and atmosphere. The mission's primary instrument was the Active Microwave Instrument (AMI), which combined a synthetic aperture radar (SAR) with a wind scatterometer (ESCAT). Additional payload elements included a radar altimeter, along-track scanning radiometer, precise range and range-rate equipment, and a laser retro-reflector. Originally designed for a nominal lifetime of three years, ERS-1 significantly exceeded expectations, operating successfully until March 2000. The mission concluded after nearly nine years of service following a failure in the spacecraft's attitude control system. The ERS-2 satellite, launched on 21 April 1995, served as a follow-on mission. It carried an almost identical payload to ERS-1, with the addition of an atmospheric ozone sensor. ERS-2 remained operational for 16 years and was decommissioned in July 2011. Together, ERS-1 and ERS-2 established a 20-year global archive of scatterometer backscatter measurements. Both satellites operated in a sun-synchronous orbit with an altitude of approximately 785 km and an inclination of 98.5°. The nominal orbital period was about 100 minutes. The ascending node crossing time was 22:15 local mean time (LMT) for ERS-1 and 22:30 LMT for ERS-2. Each mission employed a 35-day standard orbit repeat cycle, with ERS-1 additionally supporting 3-day and 168-day repeat cycles for specific mission phases. An overview of key mission parameters is provided in Table 3.1.

Mission parameter	**Unit**	**ERS-1**	**ERS-2**
Launch date	–	1991-07-17	1995-04-21
Spacecraft mass	[kg]	2 384	2 516
ESCAT payload mass	[kg]	1 100	1 100
Ground velocity	[km/s]	7	7
LMT at ascending node	–	22:15	22:30
Orbit type	–	sun-synchronous	sun-synchronous
Orbit height	[km]	782–785	782–785
Repeat cycle	[orbits]	43 501 2411	501
	[days]	3 35 168	35
Orbits/day	–	14.333 14.314 14.351	14.314

Table 3.1: ERS-1/2 mission parameter overview

3.2 Instrument description

The Active Microwave Instrument (AMI) formed the core of the ERS payload. It was designed as a multi-mode radar system operating at 5.3 GHz (C-band), integrating the functions of a high-resolution Synthetic Aperture Radar (SAR) and a lower-resolution wind scatterometer (ESCAT) [3]. The AMI supported distinct operational modes: image mode and wave mode for SAR acquisitions, and wind mode for scatterometry. Due to the high power consumption and data rate associated with SAR imaging, image and wind modes were mutually exclusive. However, a wind/wave mode enabled sequential switching between wind and wave modes, allowing for concurrent observations of ocean surface wind and wave fields. In wind mode, AMI functioned as a scatterometer, acquiring backscatter measurements using three fan-beam antennas with vertical polarization (VV). These antennas were oriented as follows:

- **Fore-beam**: 45° forward-looking relative to the satellite ground track,
- **Mid-beam**: 90° right-looking,
- **Aft-beam**: 135° backward-looking.

The three beams illuminated a swath approximately 500 km wide (see Figure 3.1). The scatterometer transmitted rectangular radio frequency (RF) pulses with durations of 130 µs for the fore- and aft-beams and 70 µs for the mid-beam. The three antennas were operated in a repeating sequence of 32 RF pulses per beam, starting with the fore-beam. The pulse repetition frequency (PRF) was set to 98 Hz for the fore- and aft-beams, and 115 Hz for the mid-beam, resulting in a full cycle, referred to as an FMA sequence, lasting 940.84 ms. Four consecutive FMA sequences corresponded to 3.763 s, covering approximately 25 km along the satellite ground track. Within each 32-pulse sequence per beam:

- **4 internal calibration pulses** were recorded. These pulses were replicas of the transmitted signal, routed through the receiver chain to monitor transmit power and receiver gain, ensuring instrument stability throughout the mission.
- **28 noise measurements** were acquired to characterize system noise, accounting for thermal background radiation and improving the signal-to-noise ratio of the backscatter signal.

An analog-to-digital converter (ADC) sampled the echo signals, calibration pulses, and noise measurements at 30 kHz. For the mid-beam, this sampling rate translated to an across-track spatial resolution of approximately 32.4 km at an incidence angle of 18°, and 14 km at 45.5° [4]. An overview of the ESCAT technical parameters is provided in Table 3.2.

3.3 Ground processing

The sampled echo signals, internal calibration pulses, and noise measurements were stored onboard using tape recorders following initial onboard processing. These data packages were subsequently downlinked to ground stations, along with supporting data such as orbit and attitude information and relevant instrument parameters, to enable the required system performance through further on-ground processing. The ground processing chain comprised several key steps:

1. **Internal calibration and signal correction:**
   The first processing step aimed to enhance the signal-to-noise ratio (SNR) and correct for fluctuations in the transmitter and receiver chains, using the recorded internal calibration data.
2. **Conversion to normalized radar cross section (σ^0):**
   The processed power echo samples were then converted to the normalized radar cross section (σ^0). This conversion utilized predetermined normalization factors, which represented the power input corresponding to a reference backscatter coefficient of unity at the Earth's surface. The normalization factors were geometry-dependent and provided as look-up tables (LUTs) for each antenna beam along the orbit.
3. **Spatial filtering and gridding:**
   To improve radiometric resolution and achieve the desired point target response, a spatial filter was applied to the σ^0 samples. The resulting values were mapped onto a predefined grid of nodes covering the entire swath:
   - The central node of the swath was defined by the intersection of the mid-beam boresight with the Earth's surface.
   - Additional nodes were placed at 25 km intervals in the across-track direction, extending from the central node toward the swath edges, along a line perpendicular to the satellite ground track.
   - This process was repeated every four FMA sequences ($\sim$3.763 s), corresponding to an along-track node spacing of 25 km.

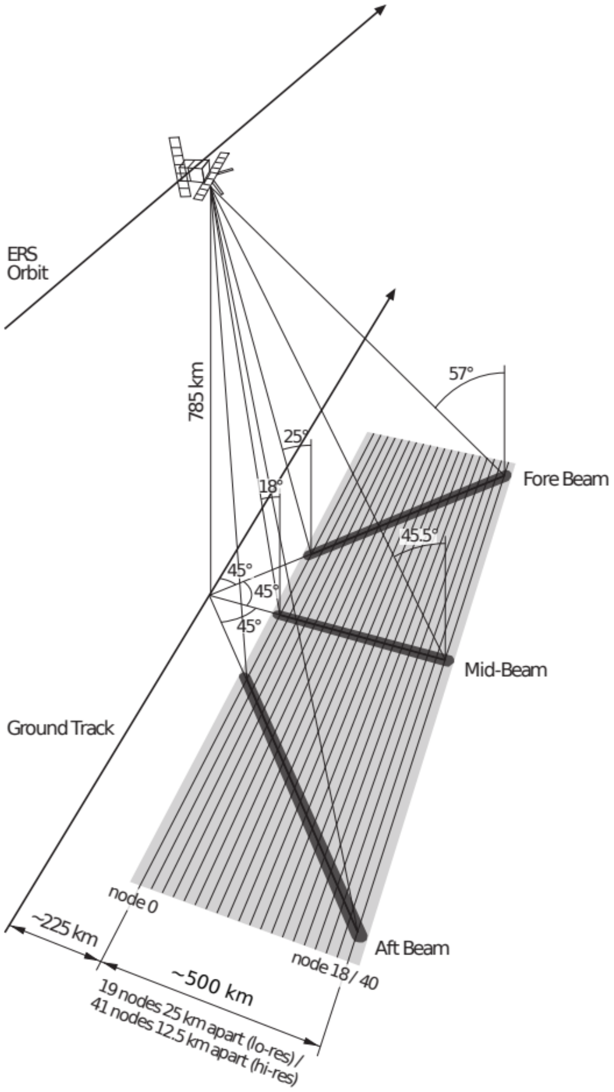

Figure 3.1: Geometrical instrument configuration and resulting orbit grid representation of ERS ESCAT. (Figure adapted from [5]).

4. **Weighted averaging using a Hamming function:**
   For each antenna beam, σ^0 samples within a defined area around each node were averaged in both along-track and across-track directions. A Hamming function was used to apply weights to the σ^0 samples based on their distance from the target node. This step was critical, as it influenced both the characteristics of the resulting σ^0 values and the effective spatial resolution of the final product.

The final output of this processing stage was a set of σ^0 triplets—one σ^0 value per antenna beam, assigned to each node in the swath. A detailed description of the ERS-1/2 ESCAT ground processing chain is provided in [4] and [6].

Instrument parameter	**Unit**			**Value**
Frequency	[GHz]			5.3
Wavelength	[cm]			5.66
Band	–			C-band
Polarization	–			VV
Swath width	[km]			500
Swath offset	[km]			200
Beam resolution	–			Range gate
Spatial resolution	[km]			25/50
Radiometric resolution	[%]			6.5–7
Dynamic range	[dB]			42
Detection bandwidth	[kHz]			25
Peak power pulse	[W]			4800
Number of pulses per 50 km	–			256
		fore	**mid**	**aft**
Incidence angle	[deg]	25–59	18–47	25–59
Antenna angle	[deg]	45	0	−45
Antenna length	[m]	3.6	2.5	3.6
Pulse duration	[µs]	130	70	130
Pulse repetition interval	[ms]	10.21	8.70	10.21
PRF	[Hz]	98	115	98
Return echo window duration	[ms]	3.93	2.46	3.93
Sampling rate	[kHz]	30	30	30
Number of bits for I/Q	–	8	8	8
Number of samples – Echo signal	–	118	74	118
Number of samples – Calibration pulse	–	30	30	30
Number of samples – Noise	–	32	32	32

Table 3.2: ESCAT technical parameter overview

4 Retrieval of backscatter observables

4.1 Pre-processing

The retrieval algorithm described in the following sections is based on the high-resolution ERS-2 Scatterometer Level 2.0 products (`ERS.ASPS20.H`), developed in ESA's SCIRoCCo project from 2014 to 2017. These products serve as the primary input for deriving the FDR4LDYN data record.

1. In the first step, the scatterometer observations were spatially resampled to a fixed Earth grid using a nearest-neighbor approach. The target grid is a Fibonacci grid with a spatial sampling distance of 12.5 km, chosen for its favorable geometric properties and consistency with existing ASCAT products.

2. Following resampling, a comprehensive quality assessment was carried out. Measurements with compromised quality were filtered based on an evaluation of the available instrument flags.

3. Subsequently, quality control measures were applied to address known inconsistencies and instrument-related effects. This included the identification of breaks and trends in the data record, which were

mitigated through intra-calibration across the different antenna beams of the ERS sensors, ensuring internal consistency of the backscatter measurements over time and across viewing geometries.

4. As a final pre-processing step, inter-calibration with Metop-A ASCAT was performed to enable seamless integration and comparability with the follow-on mission. This step ensured that the ERS backscatter data are harmonized with the ASCAT reference and are suitable for combined use in long-term applications.

In addition, synthetic ESCAT datasets were generated by sub-sampling ASCAT data to match the lower temporal resolution of the ERS missions. These experiments helped to identify necessary adaptations in the retrieval of backscatter-derived observables when working with sparser temporal sampling. Insights from this analysis informed the design of the final FDR4LDYN data processing chain. A detailed discussion of these pre-processing steps and analyses is provided in a dedicated `Quality Assessment, Quality Control, and ASCAT Interoperability Report` [7].

4.2 Correction of azimuth angle dependency

The backscatter signal is influenced by both surface properties – such as dielectric characteristics, roughness, and vegetation cover – and the measurement geometry. In particular, the backscattering coefficient varies with the incidence angle θ and the azimuth angle ϕ, the latter describing the orientation of the satellite's line of sight relative to the surface. In certain regions, notably mountainous terrain and sandy deserts, azimuthal effects can be especially pronounced due to directional surface features. These anisotropic scattering behaviors are corrected using a polynomial adjustment to the backscatter signal, following the method proposed by [8].

The azimuth angle under which a location is observed depends on the sensor's beam (Fore, Mid, or Aft) and the satellite's orbit direction (ascending or descending). For ASCAT, there is an additional distinction between left and right swath, resulting in twelve unique azimuth configurations (ϕ_i with $i \in [1, 12]$). For ESCAT, which collects data only from the right swath, there are six such configurations (ϕ_i with $i \in [1, 6]$). For each configuration, the incidence angle dependence of backscatter is modeled using a second-order polynomial. These polynomials form the basis for correcting azimuthal anisotropy in the backscatter signal:

$$\sigma_i^0(\theta) = A_i \cdot (\theta - 40)^2 + B_i \cdot (\theta - 40) + C_i \tag{1}$$

The coefficients of the six second-order polynomials (A_i, B_i, C_i) are determined by fitting each polynomial to all observations within the corresponding azimuth configuration (e.g., all measurements from the right fore beam in ascending orbit). In the current ASCAT processing, an additional global reference model ($i = 13$) is fitted using all available observations across viewing geometries. This model serves as the baseline against which individual azimuth configurations are corrected. However, since ESCAT provides only six azimuth configurations, compared to twelve in ASCAT, a different approach is required going forward. To ensure consistency and interoperability, the reference polynomial has been redefined based on a specific viewing geometry: the mid-beam of the right swath. This geometry is consistently available in both ESCAT and ASCAT datasets. The implications of this revised reference selection are still under evaluation, and a final decision will be documented in a future update of the ATBD. In addition, the choice between using ascending or descending passes as the reference direction remains open and will be resolved based on ongoing analysis.

For ESCAT, this results in a total of $3 \times 6 = 18$ static polynomial coefficients. In previous ASCAT processing, the difference between the polynomial of each viewing configuration and the global reference was used to apply a static correction to the backscatter signal. However, this approach assumes that the angular scattering behavior of land targets remains stable over long periods – a condition that does not hold in all regions. For example, urban expansion can introduce new directional reflectors (e.g., building edges), and vegetation changes along the margins of arid regions, such as those observed in the Sahel [9], may alter backscatter characteristics over time [8]. To address these limitations, the updated correction method introduces dynamic reference polynomials. As before, six azimuth configuration subsets are defined. However, in the dynamic approach, a separate second-order polynomial is fitted for each year using a five-year rolling window (± 2 years). This approach yields a total of 126 sets of polynomial coefficients (6 configurations × 21 years). These dynamic coefficients are then used in the yearly azimuth normalization procedure, ensuring that long-term changes in backscatter behavior are properly accounted for. A schematic illustration of the azimuthal correction procedure, using an example for a yearly subset and an incidence angle of 40°, is shown in Figure 4.1.

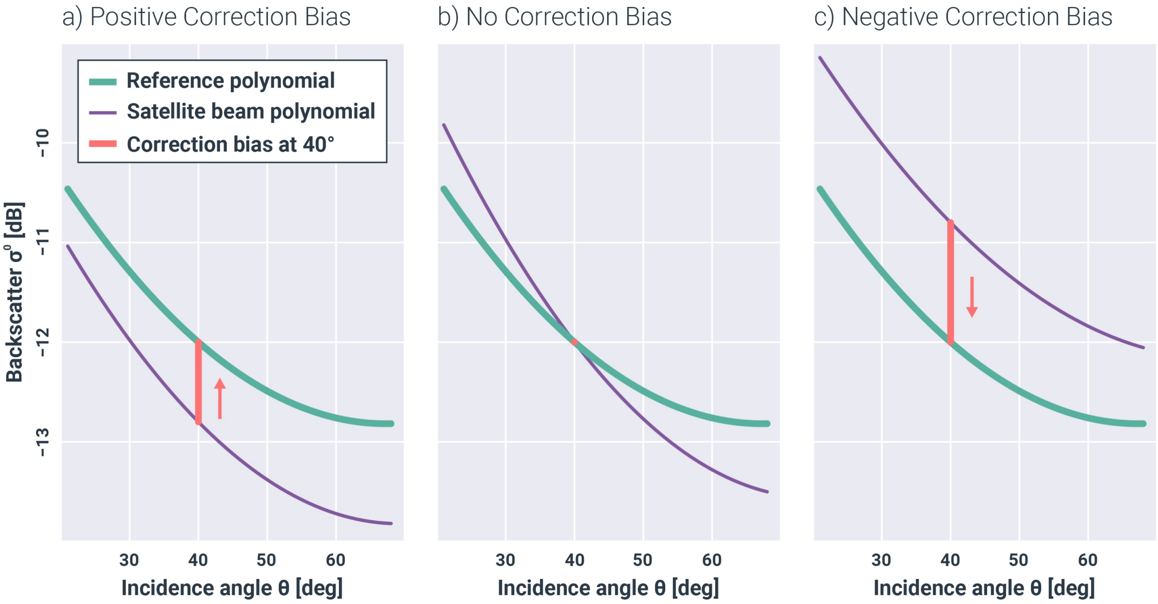

Figure 4.1: Procedure for calculating correction biases through second-order polynomials for three specific satellite beam measurements along with the static reference polynomial derived from the entire dataset. The correction bias for a point at a given incidence angle is determined by the difference between these functions and can be positive (a), zero at intersection points (b), or negative (c). This procedure is consistently applied across all six combinations of fore/mid/aft beams, and ascending/descending orbits. (Figure from [10]).

This way, the individual incidence angle dependencies of backscatter are adjusted to a common reference, mitigating azimuth effects:

$$\hat{\sigma}^0_{i,y}(\theta) = \sigma^0_{i,y}(\theta) + (A_{ref,y} - A_{i,y}) \cdot (\theta - 40)^2 + (B_{ref,y} - B_{i,y}) \cdot (\theta - 40) + (C_{ref,y} - C_{i,y}) \quad (2)$$

where $\hat{\sigma}^0_{i,y}$ represents the corrected backscatter for each configuration i and yearly subset y. The following step is using the corrected backscatter, and formulas are written without the hat ˆ nomenclature.

4.3 Estimated standard deviation (ESD) of backscatter

The Estimated Standard Deviation (ESD) represents a measure of measurement noise in the backscatter signal and is expressed in decibels (dB). The ESD is derived from the Fore and Aft beam measurements

(σ_f^0 and σ_a^0) based on the following observation: all three beams observe the same surface target within a short time interval, and the Fore and Aft beams, in particular, do so at nearly identical incidence angles. Therefore, in the absence of azimuthal effects, the Fore and Aft measurements are expected to be statistically comparable – that is, drawn from the same underlying distribution. Hence, the expectation of the difference

$$\delta := \mathrm{E}\left[\sigma_f^0 - \sigma_a^0\right] = 0 \tag{3}$$

should be zero, and the variance of this difference can be expressed as twice the variance of one of the beams (i.e $\mathrm{Var}\left[\delta\right] = 2 \cdot \mathrm{Var}\left[\sigma^0\right]$). This can be derived using error propagation and neglecting higher-order terms:

$$\mathrm{Var}\left[\delta\right] \approx \mathrm{Var}\left[\sigma_f^0\right] \cdot \left(\frac{\partial\delta}{\partial\sigma_f^0}\right)^2 + \mathrm{Var}\left[\sigma_a^0\right] \cdot \left(\frac{\partial\delta}{\partial\sigma_a^0}\right)^2 + 2 \cdot \mathrm{Cov}(\sigma_f^0, \sigma_a^0) \cdot \left(\frac{\partial\delta}{\partial\sigma_f^0}\right) \cdot \left(\frac{\partial\delta}{\partial\sigma_a^0}\right) + \dots,$$

whereby the third term is zero under the assumption of i.i.d. (independent and identically distributed random variables):

$$\mathrm{Var}\left[\delta\right] \approx \mathrm{Var}\left[\sigma_f^0\right] \cdot (1)^2 + \mathrm{Var}\left[\sigma_a^0\right] \cdot (-1)^2 + 0 \tag{4}$$

Assuming equal variances for the fore- and aft-beam, we obtain:

$$\mathrm{Var}\left[\delta\right] \approx \mathrm{Var}\left[\sigma_f^0\right] + \mathrm{Var}\left[\sigma_a^0\right] = 2 \cdot \mathrm{Var}\left[\sigma^0\right] \tag{5}$$

The previous equation can be rewritten to find the final formula for the ESD:

$$\mathrm{ESD}\left[\sigma^0\right] = \sqrt{\frac{\mathrm{Var}\left[\delta\right]}{2}} \tag{6}$$

The ESD is computed after strong outliers (defined as $\delta > Q3 + 3 \times \mathrm{IQR}$ or $\delta < Q1 - 3 \times \mathrm{IQR}$) have been removed.

4.4 Estimation of slope and curvature

In general, backscatter measurements over land show a strong dependence on the incidence angle, and a linear function (defined in the dB domain) is usually deemed sufficient to describe this relationship. The backscatter coefficient at an arbitrary incidence angle σ^0 (in dB) can be modelled as:

$$\sigma^0\left(\theta\right) = \sigma^0\left(40\right) + \sigma' \cdot \left(\theta - 40\right) \tag{7}$$

where 40° is the reference incidence angle, $\sigma^0\left(40\right)$ denotes the backscatter at this reference angle (in dB), and σ' represents the slope of the backscatter–incidence angle relationship (in dB/degree). For most land cover types, this linear approximation is valid due to the characteristic decrease in backscatter with increasing incidence angle. However, in cases where volume scattering becomes significant, such as in vegetated or snow-covered regions, the backscatter curve may flatten or deviate from linearity at higher incidence angles. To capture such non-linear behavior, a second-order polynomial is introduced, incorporating a curvature term σ'':

$$\sigma^0\left(\theta\right) = \sigma^0\left(40\right) + \sigma' \cdot \left(\theta - 40\right) + \frac{1}{2} \cdot \sigma'' \cdot \left(\theta - 40\right)^2 \tag{8}$$

From a mathematical perspective, Equation 8 represents a Taylor polynomial, as it approximates the backscatter function using a finite sum of its derivatives evaluated at a single point. In this case, the reference incidence angle of 40° serves as the expansion point. The first derivative, σ' (in dB/degree), and the second derivative, σ'' (in dB/degree^2), correspond to the slope and curvature of the backscatter–incidence angle relationship at this reference point. Once these parameters are known, the Taylor polynomial can be used to estimate backscatter values at nearby incidence angles. Conversely, by rearranging Equation 8, the backscatter at the reference incidence angle, $\sigma^0(40)$, can be inferred from a measurement taken at an arbitrary incidence angle θ.

Several methods have been developed to estimate σ' and σ'' over time, all of which are based on the concept of local slope computation [11]. A local slope provides an instantaneous estimate of the incidence angle dependency of backscatter, derived from differences in the measured signal across beams. Specifically, $\sigma^0_f - \sigma^0_m$ and $\sigma^0_a - \sigma^0_m$ can be used, since the Fore and Aft beams observe the target at the same incidence angle (i.e., $\theta_f = \theta_a$):

$$\sigma'_{fm} = \frac{\sigma^0_m - \sigma^0_f}{\theta_m - \theta_f}, \quad \sigma'_{am} = \frac{\sigma^0_m - \sigma^0_a}{\theta_m - \theta_a} \tag{9}$$

where σ'_{fm} and σ'_{am} represent slope estimates at the local incidence angle midpoints between the Mid and Fore beams, and the Mid and Aft beams, respectively:

$$\theta_{fm} = \frac{\theta_m + \theta_f}{2}, \quad \theta_{am} = \frac{\theta_m + \theta_a}{2} \tag{10}$$

If a sufficiently large and well-distributed sample of local slope estimates is available across the full range of incidence angles, a first-order approximation of $\sigma'(\theta)$ can be used to estimate the slope σ' and curvature σ'' at 40° via linear regression:

$$\sigma'(\theta) = \sigma' + \sigma'' \cdot (\theta - 40) \tag{11}$$

4.4.1 Kernel smoother method

The selection and weighting of local slope values used in the regression model have evolved over time, influenced by both data availability and computational considerations. A detailed overview of past implementations can be found in [11]. The approach to estimating σ' and σ'' currently being used in ASCAT processing is based on a Kernel Smoother (KS) method [12]. This implementation allows slope and curvature parameters to be estimated either as a climatology (i.e., one value per day of year, totaling 366 values) or as a daily time series.

For the climatology, regression coefficients are computed for each day of year d_0 by selecting local slope values from all years within a symmetric time window of ±21 days around d_0, resulting in a total kernel width of $\lambda = 42$ days. In contrast, for the dynamic time series-based estimation of slope and curvature, insights from the synthetic ESCAT experiment (see subsection 4.1) revealed the need for a wider time window in data-sparse regions and periods, particularly after the ERS-2 tape recorder failure. Unlike the climatology approach, which draws from multiple years, the dynamic method is restricted to observations within the time window of the given date alone. This limitation reduces data availability and makes the method more sensitive to temporal gaps. The narrower ±21-day window for dynamic slope and curvature used in ASCAT processing was found to introduce noisy estimates, frequent data gaps, and strong edge effects in such conditions in the case of ESCAT data. To mitigate these issues, we adopted a wider window of ±42 days (i.e., $\lambda = 84$ days) for ESCAT, improving temporal robustness in sparse periods.

For simplicity, the following description focuses on the climatology-based computation. The dynamic estimation follows the same principle but is applied to each individual day in the measurement time series rather than to a fixed day of year. It uses only data within the time window centered on the specific date, rather than drawing from all available years.

Within the selected time window, local slope values are weighted according to their temporal distance from d_0 using the Epanechnikov kernel function (see [13] and Figure 4.2, Chapter 6):

$$k(d_0, d) = D\left(\frac{d - d_0}{\lambda}\right) \tag{12}$$

with

$$D(t) = \begin{cases} \frac{3}{4} \cdot (1 - t^2) & \text{if } |t| \leq 1 \\ 0 & \text{else} \end{cases} \tag{13}$$

The Epanechnikov kernel has finite support over the interval $[-\lambda, \lambda]$ and is normalized to integrate to one. The kernel width λ is a key parameter that controls the balance between bias and variance in the estimate: increasing λ reduces the variance by incorporating more observations but simultaneously increases the bias due to the inclusion of more distant (and potentially less representative) data points.

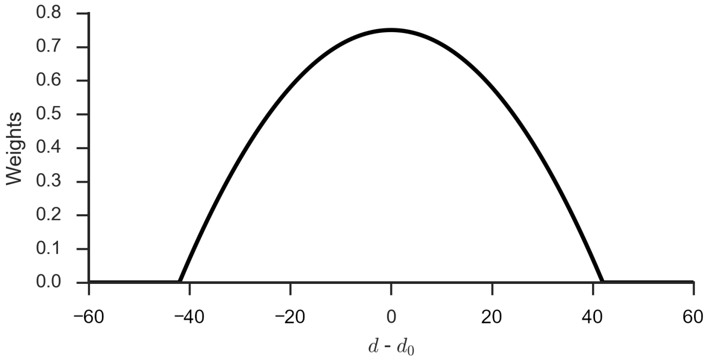

Figure 4.2: Example of the Epanechnikov kernel (λ = 42).

Typically, a kernel function is defined over the independent variable – in this case, the incidence angle θ. However, since the goal here is to estimate the coefficients of the linear approximation (Equation 11) across the full incidence angle range for a specific day of year d_0, the kernel is instead defined over time. More precisely, it acts as a function of the day of year. All local slope values falling within the interval $|(d - d_0)/\lambda| \leq 1$ are included in the weighted linear regression and are weighted based on their temporal distance to d_0, as defined by the Epanechnikov kernel (see Equation 14).

Let $\mathbf{x} \in \mathbb{R}^N$ and $\mathbf{y} \in \mathbb{R}^N$ denote the vectors containing the incidence angles θ_l and corresponding local slope values σ'_l for all N observations within the kernel support around day d_0. Define the design matrix $\mathbf{A} \in \mathbb{R}^{N\times 2}$ such that its first column consists of ones and its second column corresponds to $\mathbf{x}$. Let $\mathbf{W}(d_0) \in \mathbb{R}^{N\times N}$ be a diagonal weight matrix, where the i-th diagonal entry is given by the kernel weight for the i-th observation, i.e., $\mathbf{W}(d_0)[i, i] = k(d_0, d_i)$. Then, the estimates for σ' and σ'' at day d_0 are obtained as:

$$\begin{pmatrix} \sigma'(d_0) \\ \sigma''(d_0) \end{pmatrix} = (\mathbf{A}^T \mathbf{W}(d_0)\mathbf{A})^{-1}\mathbf{A}^T \mathbf{W}(d_0)\mathbf{y} = \mathbf{B}\mathbf{y} \tag{14}$$

If the error covariance of the local slope values used in the fit is given by $\mathbf{\Sigma}_l$, then the error covariance of the parameters is given by:

$$\mathbf{\Sigma}_{\sigma',\sigma''} = \mathbf{B}\mathbf{\Sigma}_{\mathbf{l}}\mathbf{B}^T \tag{15}$$

At the moment, it is assumed that $\mathbf{\Sigma}_{\mathbf{l}}$ is homeoscedastic (i.e., the errors for all local slope values have the same variance s_l^2) and the errors are uncorrelated: $\mathbf{\Sigma}_{\mathbf{l}} = \mathbf{I}s_l^2$, and estimate s_l^2 from the residuals of the fit (in order to avoid confusion with σ for the representation of backscatter, the variance notation is s^2).

4.4.2 Regularization method

In addition to the kernel smoother approach, a regularization-based method was developed to better represent the dynamics of slope and curvature at short time scales [14]. To estimate slope and curvature using the regularization method, the same local slopes (Equation 9) and local incidence angles (Equation 10) are used as in the kernel smoother method. All available values of the local slopes and incidence angles are used in one single estimation for each grid point. Instead of applying weights to the observations, the first differences of the estimated slope and curvature time series are constrained by including a first difference matrix ($\mathbf{C}$) and a scalar driving the magnitude of the constraint (γ) in the estimation equation. The equation to estimate the full time series of slope (σ') and curvature (σ'') per grid point becomes:

$$\begin{pmatrix} \sigma' \\ \sigma'' \end{pmatrix} = (\mathbf{A}^T\mathbf{A} + \gamma^2\mathbf{C}^T\mathbf{C})^{-1}\mathbf{A}^T\mathbf{y} \tag{16}$$

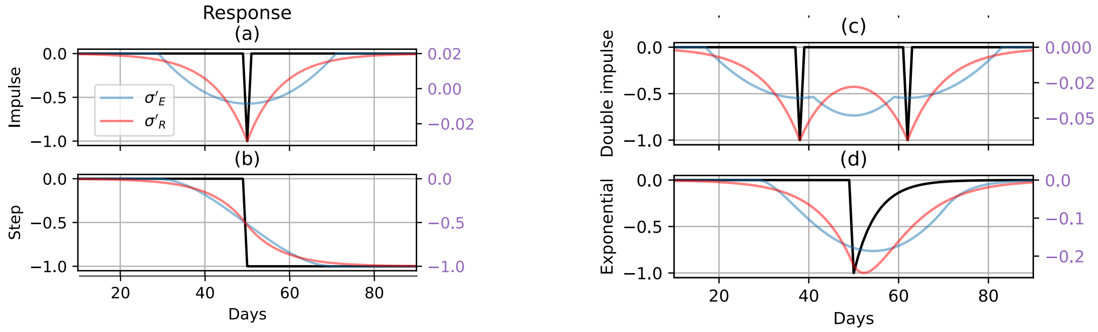

Figure 4.3: Response of kernel smoother (blue) and regularization method (red) to an impulse shown in black: single impulse (a), step (b), double impulse (c) functions, and a step followed by an exponential decay (d). The regularization response is computed with $\gamma = 8$, and the kernel smoother response is computed with a 21-day half-width. Purple axes correspond to the values of the regularization and Epanechnikov responses. Black axes denote the values of the input functions. Figure adapted from [14].

Applying a constraint on the dynamics of the estimated time series, instead of a kernel-based approach, results in a better correspondence between the timing of changes in the observations, and timing of changes in the estimated parameters. Figure 4.3 illustrates the difference between the responses of the kernel smoother and the regularization method to a simplified input signal. The timing of the changes in the regularized time series shows a better correspondence to the changes in the input signal. A more elaborate description and comparison of the estimation method can be found in [14].

4.4.3 Empirical Bayesian method

An additional alternative, an empirical Bayesian method, is currently under development and will be described in a future version of this document. This approach is planned as a further extension of the current kernel smoother method to enhance the robustness and flexibility of slope and curvature estimation.

4.5 Interpolation to reference incidence angle

Once $\sigma'(d)$ and $\sigma''(d)$ have been computed on a daily basis d, the incidence angle interpolation can be applied to the backscatter measurements of each beam b (Fore, Mid, Aft) using:

$$\sigma^0_b(40) = \sigma^0_b(\theta_b) - \sigma'(d) \cdot \Delta\theta_b - \frac{1}{2} \cdot \sigma''(d) \cdot \Delta\theta_b^2 \tag{17}$$

with $\Delta\theta_b = \theta_b - 40$. The backscatter observations of the three beams interpolated to a common reference angle are averaged:

$$\bar{\sigma}^0(40) = \frac{1}{3} \cdot \sum_{b \in \{f,m,a\}} \sigma^0_b(40) \tag{18}$$

which gives the final backscatter $\bar{\sigma}^0(40)$ interpolated at the reference incidence angle. The noise variance of the interpolated backscatter at the reference incidence angle for each beam b is given by:

$$\mathrm{Var}\left[\sigma^0_b(40)\right] = \mathrm{ESD}\left[\sigma^0\right]^2 + \mathrm{Var}\left[\sigma'(d)\right] \cdot \Delta\theta_b^2 + \frac{1}{4} \cdot \mathrm{Var}\left[\sigma''(d)\right] \cdot \Delta\theta_b^4 \tag{19}$$

and after averaging, the noise variance reduces to:

$$\mathrm{Var}\left[\bar{\sigma}^0(40)\right] = \frac{1}{9} \cdot \sum_{b \in \{f,m,a\}} \mathrm{Var}\left[\sigma^0_b(40)\right] \tag{20}$$

Slope and curvature derived using the regularization method described in subsubsection 4.4.2 are likely the most suitable choice for normalizing backscatter. This is because they better reflect the timing of changes observed in the backscatter signal. Further tests will be conducted during the course of the project to confirm this assumption. Any resulting decisions will be documented in future updates of the ATBD.

4.6 Known signal characteristics and contextual factors

The FDR4LDYN data record provides consistent, calibrated backscatter, slope, and curvature observations over global land surfaces. However, the backscatter signal is inherently influenced by a range of geophysical and observational factors, particularly in complex environments such as dense forests, snow-covered or frozen soils, open water bodies, wetlands, and urban areas. In these cases, the signal may exhibit behaviors that differ from typical land surface scattering and may require careful interpretation. While these effects do not compromise the integrity of the backscatter observations themselves, they can affect the stability and interpretability of derived downstream variables. Users are therefore encouraged to consider ancillary datasets when analyzing time series in such regions. Additionally, the dynamic nature of azimuthal anisotropy, subsurface scattering, and seasonal transitions should be taken into account when assessing temporal changes. These considerations are particularly relevant for applications that use FDR4LDYN products as input to further retrieval algorithms, including soil moisture estimation or vegetation dynamics monitoring.

4.6.1 Vegetation

In densely vegetated regions, such as tropical rainforests, C-band microwaves are largely attenuated by the canopy and do not reach the soil surface. As a result, the backscatter signal carries little to no soil information and typically exhibits very low temporal variability, reflecting limited signal sensitivity to changes in surface conditions.

4.6.2 Desert areas

Desert regions are defined by extremely low soil moisture levels, driven by minimal annual precipitation. As a result, the backscatter signal in these areas is typically weak and exhibits limited temporal variability. In particular, sandy deserts can show backscatter values below -20 dB. These environments are also more susceptible to azimuthal anisotropy and Bragg scattering effects [15]. The latter arises from small-scale surface ripples on sand dunes, which can enhance the backscatter signal for specific incidence angle ranges due to coherent scattering mechanisms. Such effects may introduce directional biases and should be considered when interpreting backscatter, slope, and curvature in arid landscapes.

4.6.3 Subsurface scattering

In arid regions, particularly where soils are very dry, subsurface volume scattering can become a dominant component of the backscatter signal. Under such conditions, the penetration depth of C-band microwaves can reach up to several meters, increasing the likelihood of interactions with buried layers such as bedrock. This phenomenon is especially notable in parts of North Africa, where it can lead to an inverse relationship between backscatter and surface soil moisture. During dry periods, the signal may originate from deeper, reflective subsurface layers, resulting in unexpectedly high backscatter values despite a dry surface. Conversely, during wet periods, the increased surface moisture reduces the penetration depth, limiting the signal's interaction with deeper layers and thus lowering the backscatter. This effect can confound soil moisture retrieval algorithms, which may falsely interpret increasing backscatter during dry-down as a rise in surface moisture [16]. While such misinterpretations are not relevant for the FDR4LDYN product series itself, they should be considered when using the dataset as input for downstream applications.

4.6.4 Snow

The backscatter signal in snow-covered regions is influenced by a range of snowpack properties, including liquid water content, grain size and shape, snow depth and layering, as well as the roughness of the air–snow interface. Depending on these factors, different scattering mechanisms may dominate, such as surface scattering, volume scattering within the snowpack, or reflection from the underlying soil surface if penetration is sufficient. These complex interactions often reduce the interpretability of the backscatter signal during snow-covered periods. To support the identification of such conditions, a dynamic snow cover flag is included in the FDR4LDYN product. This flag is derived from auxiliary land surface model data provided by the ERA5-Land reanalysis [17] and enables users to mask time periods affected by snow cover.

4.6.5 Frozen soil

When soil temperatures fall below 0°C, the dielectric properties of the soil change significantly. As the water in the soil freezes, its molecules can no longer respond to the incoming microwave signal, leading to a marked reduction in backscatter. This freezing effect complicates interpretation, particularly in vegetated areas where plant structures may adapt to cold conditions and partially mask or alter the signal response. To help mitigate these effects, the FDR4LDYN product includes a dynamic frozen soil flag, also based on ERA5-Land temperature data. Users are advised to apply this flag to exclude periods where frozen conditions may impair the reliability of the backscatter signal, depending on their desired application.

4.6.6 Surface water and wetlands

In areas with surface water or wetlands, the backscatter signal is primarily governed by surface roughness, as C-band microwaves penetrate only the uppermost 1–2 mm of the water surface. Calm, open water behaves like a specular reflector, directing most of the incoming energy away from the satellite sensor and resulting in very low backscatter values. When surface winds generate small waves, the roughness increases, leading to enhanced backscatter in the upwind and downwind viewing directions, while the signal remains low in crosswind directions. This anisotropic behavior should be considered when interpreting backscatter measurements over water bodies and inundated areas, especially in the context of wind-induced variability or seasonal flooding.

4.6.7 Topographic complexity

In mountainous and topographically complex regions, backscatter signals often exhibit high spatial and temporal variability. This variability arises from local differences in slope, aspect, and elevation, which affect the incidence angle and scattering geometry of the microwave signal. Since the FDR4LDYN retrieval algorithm does not explicitly account for terrain-induced effects, users should interpret backscatter, slope, and curvature values in such areas with caution.

4.6.8 Urban areas

In urban and suburban regions, the backscatter signal may be strongly affected by built structures and heterogeneous land cover. Buildings and other man-made features can introduce distinct scattering mechanisms, such as double or multiple reflections between vertical and horizontal surfaces. These effects are highly directional and can result in unusually high backscatter in specific viewing geometries. Even at the coarse spatial resolution of ESCAT, strong responses from isolated point-like targets can dominate the footprint-level signal [8]. As a result, urban areas may exhibit sharp backscatter peaks and increased anisotropy, which should be carefully considered when interpreting the data in such environments.

4.6.9 Radio frequency interference

The occurrence of radio frequency interference (RFI), especially near urban areas, presents an additional challenge, as ESCAT's frequency range began to be shared with mobile telecommunication services starting in 2003. However, recent studies indicate that RFI became a significant issue in Metop ASCAT data only after the end of the ERS-2 mission in 2011. Therefore, the impact of RFI on ESCAT measurements is expected to be negligible.

5 References

[1] Vass, P., European Space Agency, Earthnet, and European Space Research Institute, *ERS-1 System* (ESA SP 1146). Noordwijk, Netherlands: ESA Publications Division, 1992.

[2] European Space Agency, *Earthnet online - the ers missions*, https://earth.esa.int/eogateway/missions/ers, Accessed on 10 June 2025, 2025.

[3] Attema, E., "The active microwave instrument on-board the ers-1 satellite," *Proceedings of the IEEE*, vol. 79, no. 6, pp. 791–799, 1991. doi: 10.1109/5.90158.

[4] Lecomte, P., "Ers scatterometer instrument and the on-ground processing of its data," in *European Space Agency Special Publication*, ESA, 1998, pp. 241–260.

[5] Bartalis, Z., "Spaceborne scatterometers for change detection over land," Ph.D. dissertation, Technische Universität Wien, Vienna, Dec. 2009.

[6] Neyt, X., Pettiaux, P., and Acheroy, M., "Scatterometer ground processing review for gyro-less operations," in *Proceedings of SPIE - The International Society for Optical Engineering*, vol. 4880, 2002, pp. 1–10.

[7] ESA, *ESCAT Quality Assessment, Quality Control, and ASCAT Interoperability Report*, v1.0, 2025.

[8] Bartalis, Z., Scipal, K., and Wagner, W., "Azimuthal anisotropy of scatterometer measurements over land," *IEEE Transactions on Geoscience and Remote Sensing*, vol. 44, no. 8, pp. 2083–2092, 2006. doi: 10.1109/TGRS.2006.872084.

[9] Dardel, C., Kergoat, L., Hiernaux, P., Mougin, E., Grippa, M., and Tucker, C. J., "Re-greening sahel: 30 years of remote sensing data and field observations (mali, niger)," *Remote Sensing of Environment*, vol. 140, pp. 350–364, 2014. doi: https://doi.org/10.1016/j.rse.2013.09.011.

[10] Lindorfer, R., "Azimuthal anisotropy in ASCAT backscatter measurements," Technische Universität Wien, Vienna, Austria, 2024. [Online]. Available: https://doi.org/10.34726/hss.2024.120220.

[11] Hahn, S., Reimer, C., Vreugdenhil, M., Melzer, T., and Wagner, W., "Dynamic Characterization of the Incidence Angle Dependency of Backscatter Using Metop ASCAT," *IEEE Journal of Selected Topics in Applied Earth Observations and Remote Sensing*, vol. 10, no. 3, p. 12, 2016. doi: 10.1109/JSTARS.2016.2628523.

[12] Melzer, T., "Vegetation Modelling in WARP 6.0," in *EUMETSAT Meteorological Satellite Conference*, Vienna, Austria, 2013.

[13] Hastie, T., Tibshirani, R., and Friedman, J., *The Elements of Statistical Learning : Data Mining, Inference, and Prediction*, English. New York: Springer, 2009.

[14] Frantzen, P., Steele-Dunne, S. C., Quaife, T., Vreugdenhil, M., Hahn, S., and Wagner, W., "Improved Estimation of Temporal Dynamics in the ASCAT Backscatter-Incidence Angle Relation Using Regularization," *IEEE Journal of Selected Topics in Applied Earth Observations and Remote Sensing*, vol. 18, pp. 13 457–13 471, 2025. doi: 10.1109/JSTARS.2025.3572306. [Online]. Available: https://ieeexplore.ieee.org/document/11008820 (visited on 06/05/2025).

[15] Stephen, H. and Long, D., "Microwave backscatter modeling of erg surfaces in the Sahara desert," *IEEE Transactions on Geoscience and Remote Sensing*, vol. 43, no. 2, pp. 238–247, Feb. 2005. doi: 10.1109/TGRS.2004.840646.

[16] Wagner, W., Lindorfer, R., Melzer, T., Hahn, S., Bauer-Marschallinger, B., Morrison, K., Calvet, J.-C., Hobbs, S., Quast, R., Greimeister-Pfeil, I., and Vreugdenhil, M., "Widespread occurrence of anomalous c-band backscatter signals in arid environments caused by subsurface scattering," *Remote Sensing of Environment*, vol. 276, p. 113 025, Jul. 2022. doi: 10.1016/j.rse.2022.113025.

[17] Muñoz-Sabater, J., Dutra, E., Agustí-Panareda, A., Albergel, C., Arduini, G., Balsamo, G., Boussetta, S., Choulga, M., Harrigan, S., Hersbach, H., Martens, B., Miralles, D. G., Piles, M., Rodríguez-Fernández, N. J., Zsoter, E., Buontempo, C., and Thépaut, J.-N., "Era5-land: A state-of-the-art global reanalysis dataset for land applications," *Earth System Science Data*, vol. 13, no. 9, pp. 4349–4383, 2021. DOI: 10.5194/essd-13-4349-2021. [Online]. Available: https://essd.copernicus.org/articles/13/4349/2021/.

List of Tables

List of Figures

List of Acronyms

AMI	Active Microwave Instrument
ASCAT	Advanced Scatterometer
ATBD	Algorithm Theoretical Basis Document
DoY	Day of Year
ECMWF	European Centre for Medium-Range Weather Forecasts
ERA5-Land	ERA5-Land Surface Reanalysis from ECMWF
ERS	European Remote-sensing Satellite (1 and 2)
ESA	European Space Agency
ESCAT	ERS-1 and ERS-2 Scatterometer
ESD	Estimated Standard Deviation
FDR4LDYN	Fundamental Data Record for Land Dynamics
KS	Kernel Smoother
MetOp	Meteorological Operational Platform
RFI	Radio Frequency Interference
SAR	Synthetic Aperture Radar
SCA	Scatterometer on Metop-SG-B
SNR	Signal-to-Noise Ratio
TU Delft	Technische Universiteit Delft (Delft University of Technology)
TU Wien	Technische Universität Wien (Vienna University of Technology)
VV	Vertical Transmit and Vertical Receive Polarisation